

AIDE: Annotation-efficient deep learning for automatic medical image segmentation

Cheng Li^{1,9}, Rongpin Wang^{2,9}, Zaiyi Liu^{3,9}, Meiyun Wang^{4,9}, Hongna Tan⁴, Yaping Wu⁴, Xinfeng Liu², Hui Sun¹, Rui Yang⁵, Xin Liu¹, Ismail Ben Ayed⁶, Hairong Zheng^{1,10*}, Hanchuan Peng^{7,10*}, Shanshan Wang^{1,8,10*}

¹Paul C. Lauterbur Research Center for Biomedical Imaging, Shenzhen Institutes of Advanced Technology, Chinese Academy of Sciences, Shenzhen, Guangdong, China.

²Department of Medical Imaging, Guizhou Provincial People's Hospital, Guizhou, China.

³Department of Medical Imaging, Guangdong General Hospital, Guangdong Academy of Medical Sciences, Guangzhou, Guangdong, China.

⁴Department of Medical Imaging, Henan Provincial People's Hospital & the People's Hospital of Zhengzhou University, Zhengzhou 450003, Henan, China.

⁵Department of Urology, Renmin Hospital of Wuhan University, Wuhan, Hubei, China.

⁶ETS Montreal, Montreal, Canada.

⁷SEU-ALLEN Joint Center, Institutes for Brain and Intelligence, Southeast University, Nanjing, Jiangsu, China

⁸Pengcheng Laboratory, Shenzhen, China

⁹These authors contributed equally: Cheng Li, Rongpin Wang, Zaiyi Liu, Meiyun Wang.

¹⁰The corresponding authors are: Shanshan Wang, Hairong Zheng, Hanchuan Peng

*e-mail: ss.wang@siat.ac.cn; hr.zheng@siat.ac.cn; h@braintell.org;

Abstract

Accurate image segmentation is crucial for medical imaging applications. The prevailing deep learning approaches typically rely on very large training datasets with high-quality manual annotations, which are often not available in medical imaging. We introduce Annotation-efficient Deep Learning (AIDE) to handle imperfect datasets with an elaborately designed cross-model self-correcting mechanism. AIDE improves the segmentation Dice scores of conventional deep learning models on open datasets possessing scarce or noisy annotations by up to 30%. For three clinical datasets containing 11,852 breast images of 872 patients from three medical centers, AIDE consistently produces segmentation maps comparable to those generated by the fully supervised counterparts as well as the manual annotations of independent radiologists by utilizing only 10% training annotations. Such a 10-fold improvement of efficiency in utilizing experts' labels has the potential to promote a wide range of biomedical applications.

Diagnostic imaging is an important tool in the clinic. Various imaging modalities, such as magnetic resonance imaging (MRI) and computed tomography (CT), contribute to a powerful and effective means for the noninvasive inspection of the patient. Delineating or segmenting the regions of interest (ROIs) with the acquired images is a crucial step in the pipeline of medical image analysis. Image segmentation has found successful applications in various fields, including disease diagnosis and treatment planning¹⁻³. With the development of imaging facilities, medical image acquisition becomes faster with higher resolutions. Automated segmentation algorithms are required to assist radiologists in realizing accurate and timely imaging-based diagnosis^{4,5}.

Deep neural networks (DNNs) have been widely employed for medical image segmentation over the past decades⁶⁻¹¹. Their success relies heavily on the training data especially the annotations^{12,13}, whereas annotating medical images is time-consuming, labor-intensive, and expensive. Depending on the complexity of the ROIs to segment, and the local anatomical structures, it may take from minutes to hours to annotate one image. Besides, label noise is an inevitable issue in real-world applications of DNNs. It can result from the systematic errors of the annotator as well as inter-annotator variations. More than three domain experts are typically needed to generate trustworthy annotations. Consequently, lacking large and high-quality labeled datasets has been identified as the primary limitation to supervised deep learning for new medical imaging tasks¹⁴⁻¹⁷. Therefore, it is in need to develop new deep learning works to handle three most frequently appeared imperfect datasets, namely, those having limited annotations, those lacking target domain annotations, and those containing noisy annotations. Recent deep learning works have presented encouraging performances in handling certain types of imperfect datasets in isolation¹⁸⁻²¹ but have not yet shown general applicability by tackling all three.

In this work, we build a generally applicable deep learning framework, Annotation-efficient Deep Learning (AIDE) framework, for medical image segmentation with all the three types of imperfect datasets. A novel cross-model self-correcting mechanism is introduced, which selectively generates pseudo-labels according to an observed small loss criterion. The self-correcting of low-quality labels proceeds with alternating local label filtering steps and global label correction steps. Cross-model co-optimization is developed to effectively reduce the propagation of the same errors within single networks.

Extensive experiments on open datasets with limited, no target domain, and noisy annotations are conducted. Significantly better results are achieved with AIDE compared to the respective baselines, which validate the effectiveness of the proposed framework on processing imperfect datasets. Furthermore, three datasets for breast tumor segmentation (11,852 image samples of 872 patients) from three medical centers are utilized to evaluate the feasibility of AIDE for clinical applications. Compared to the fully supervised models and independent radiologists, comparable results are achieved with AIDE by utilizing only 10% of the training data annotations. Our results indicate that DNNs are capable of fully exploring the image contents under proper guidance without the necessity of large and high-quality annotated datasets. We believe that, with further development and clinical validations, our proposed framework has the potential to improve the medical image diagnosing workflow in an efficient manner and at a low cost.

Methods

CHAOS dataset. Abdomen MR images from the CHAOS challenge are adopted³⁸⁻⁴⁰ (Fig. 1). These images were acquired with a 1.5T Philips MRI system. The image matrix size is 256 x 256 with an inplane resolution from 1.36mm to 1.89mm. The slice thickness is between 5.5mm and

9mm. One 3D image contains 26 to 50 slices. Although multi-parametric MR images are provided, they are not registered and thus, difficult to be utilized as multi-modal inputs for the segmentation task. We utilize the T1-DUAL images that for each patient, there is one inphase image and one outphase image. They can be treated as multi-modal inputs. In total, the challenge provides data from 40 patients, 20 cases (647 T1-DUAL images, 647 samples) with high-quality annotations and 20 cases (653 T1-DUAL images, 653 samples) without annotations.

Prostate datasets. T2-weighted MR images of the prostate from two challenges (Fig. 1), NCI-ISBI 2013⁴¹ and PROMISE12⁴² are utilized. NCI-ISBI 2013 consists of three groups of data, the training set (60 cases), the test set (10 cases), and the leaderboard set (10 cases). All are provided with high-quality annotations. We combine the test set and leaderboard set to form our enlarged test set (20 cases) and divide the dataset into two datasets according to the data acquisition sites to form two domain samples. Domain 1 dataset contains training and test data collected with 1.5T MRI systems from Boston Medical Center (30 training cases and 10 test cases) and Domain 2 dataset contains data collected with 3.0T MRI systems from Radboud University Nijmegen Medical Centre (30 training cases and 10 test cases). PROMISE12 provides data from 50 patients with high-quality annotations. These samples were collected from different centers using different MRI machines with different acquisition protocols. Deleting 13 cases that are the same as those in Domain 2, 37 cases collected from Haukeland University Hospital (12 cases), Beth Israel Deaconess Medical Center (12 cases), and University College London (13 cases) are utilized. Therefore, PROMISE12 can be treated as a combined dataset from different domains, which is referred to as Domain 3 dataset for our experiments. Of the 37 cases, 27 cases are randomly selected as the training set and the remaining 10 cases forms the test set.

QUBIQ datasets. The QUBIQ challenge provides four datasets with annotations from multiple experts, including a prostate image dataset of 55 cases (6 sets of annotations), a brain growth image dataset of 39 cases (7 sets of annotations), a brain tumor image dataset of 32 cases (3 sets of annotations), and a kidney image dataset of 24 cases (3 sets of annotations). In total, there are seven binary segmentation tasks, two for prostate segmentation, one for brain growth segmentation, three for brain tumor segmentation, and one for kidney segmentation. In this study, we conduct four tasks (Fig. 1), one for each dataset, to investigate the effects of our proposed AIDE framework. Following the challenge, 48 cases of the prostate data, 34 cases of the brain growth data, 28 cases of the brain tumor data, and 20 cases of the kidney data are utilized as the training data. The remaining are the testing data.

Breast tumor datasets. This retrospective study was approved by the institutional review board of each participating hospital with the written informed consent requirement waived. All patient records were de-identified before analysis and reviewed by the institutional review boards to guarantee no potential risk to patients. The researchers who conduct the segmentation tasks have no link to the patients to prevent any possible breach of confidentiality.

Dynamic contrast-enhanced breast MR data from three medical centers, Guangdong General Hospital (GGH), Guizhou Provincial People’s Hospital (GPPH), and Henan Provincial People’s Hospital (HPPH), are included and investigated (Fig. 1). GGH provides 300 patient cases, GPPH provides 200 cases, and HPPH provides 372 cases. For each dataset, experienced radiologists with more than 10 years of experience are involved in the image annotation work. For the HPPH dataset, breast tumor regions in central slices are annotated, leading to 300 image samples. 3D breast tumor

annotations are provided for the GGH dataset and HPPH dataset, respectively. GGH dataset has 4,902 annotated image samples and HPPH contains 6,650 image samples. This resulted in a total of 872 MR data (11,852 image samples) for our experiments. For each dataset, we randomly select 100 annotated patient cases as the respective hold-out test sets and the remaining as the training sets.

AIDE framework. Fig. 1 illustrates the overall AIDE framework. Details of the proposed self-correcting method are described in Algorithm 1. Two networks are learned in parallel to achieve cross-model co-optimization and self-correcting of low-quality annotations of imperfect datasets.

The whole process can be divided into two major steps. The first is a local label filtering step. In each iteration, a defined percentage of training samples with relatively larger segmentation losses are selected by the counterpart model as suspicious samples that have low-quality annotations. For these samples, the final loss function is calculated as a weighted summation of a segmentation loss and a consistency loss. We choose the commonly utilized combination of Dice loss and cross-entropy loss as our segmentation loss in this work (equation (1)). The consistency loss is introduced as a consistency regularization to the network. Specifically, the means of the outputs of K augmented inputs are calculated, which are regarded as the pseudo-labels after temperature sharpening. Consistency loss, which is implemented with the mean square error (MSE) loss (equation (2)), is calculated between the network outputs of suspected noisy samples and the corresponding pseudo-labels. The samples with smaller segmentation losses are expected to be the accurately labeled samples, and only the segmentation loss is calculated. The network parameters are updated according to the respective losses.

The second is a global label correction step. After each epoch, the Dice similarity coefficients (DSCs) of the whole training set are calculated and ranked. A defined percentage of samples with the smallest DSCs are picked and their labels are updated when certain criteria are met. In this work, we update the labels if the training epoch number is smaller than the defined warm up epoch number or the training epoch number can be divided by 10.

$$L_{seg}(y, y') = L_{Dice}(y, y') + \alpha \cdot L_{CE}(y, y') = \left(1 - \frac{2 \cdot \sum_{i=1}^N y'_i y_{i+\varepsilon}}{\sum_{i=1}^N y'_i + \sum_{i=1}^N y_{i+\varepsilon}}\right) - \frac{\alpha}{N} (\sum_{i=1}^N y_i \log(y'_i) + (1 - y_i) \log(1 - y'_i)) \quad (1)$$

$$L_{cor}(\hat{y}, y') = \frac{1}{2N} \sum_{i=1}^N \|\hat{y}_i - y_i\|^2 \quad (2)$$

where y' is the prediction of the network, y is the reference, \hat{y} is the temperature sharpened local pseudo labels generated from the augmented inputs, N refers to the total pixels in the image, α is a constant to balance the different losses and we set $\alpha = 1$ in all our experiments unless otherwise specified, and ε is a constant to insure the numerical stability and we set $\varepsilon = 1.0$.

The rationale for our filtering and correction steps is that we observed when training data containing noisy annotations, there is a positive correlation between the DSCs calculated comparing network outputs to current noisy labels and the DSCs calculated comparing current noisy labels to the high-quality labels for the training set (Fig. 2). This phenomenon is relevant to the network memorization pattern and it has been frequently observed for natural image analysis^{35,43,44}. Here we show that the same network memorization pattern exists for medical image segmentation.

Segmentation network architectures. A simple, general and robust network architecture is designed to process the different image inputs. The architectures employs the classical encoder-decoder structure with an encoder stream to downsample image resolutions and extract image features, and a decoder stream to recover image resolutions and generate segmentation outputs⁴⁵.

Skip connections are included to help increase the localization accuracy. Since the depth resolution is much lower than the inplane resolution for the liver and prostate segmentation datasets, and the noisy datasets contain only 2D samples, all our experiments proceed in a 2D fashion. The 3D extension is straightforward but needs much more effort to construct suitable implementation datasets, which is out of the scope of this study.

Similar encoder-decoder network architectures are utilized to handle single- and multi-modal image datasets. During encoding, input images go through five downsampling blocks sequentially with four maxpooling operations in between to extract multi-layer image features. For multi-modal inputs, multiple downsampling streams are utilized to extract features from the different modalities^{46,47}. The extracted features are combined in a multi-layer fusion manner. Features from all downsampling blocks are correspondingly concatenated to fuse information from different modalities. During decoding, the extracted image features pass four upsampling blocks, each followed by a bilinear upsampling operation, to generate segmentation outputs with the same size as the inputs. Downsampling and upsampling blocks have similar components, consisting of two convolution layers with a 3x3 convolution, a batch normalization, and a ReLU activation. The low level features of the encoder are introduced to the decoder through skip connections and feature concatenation. Finally, a 1x1 convolution is appended to generate two features corresponding to the background and target segmentation maps and a Softmax activation is included to generate the segmentation probability maps.

Evaluation metrics. Different metrics are available to characterize the segmentation results. For our experiments, we choose the commonly utilized Dice score (Dice similarity coefficient, DSC), relative area/volume difference (RAVD), average symmetric surface distance (ASSD), and maximum symmetric surface distance (MSSD).

$$\text{DSC} = \frac{2TP}{2TP+FP+FN} \quad (3)$$

$$\text{RAVD} = \frac{FP-FN}{TP+FN} \quad (4)$$

$$\text{ASSD} = \frac{1}{|S(y')|+|S(y)|} (\sum_{a \in S(y')} \min_{b \in S(y)} ||a - b|| + \sum_{b \in S(y)} \min_{a \in S(y')} ||b - a||) \quad (5)$$

$$\text{MSSD} = \max\{ \max_{a \in S(y')} \min_{b \in S(y)} ||a - b||, \max_{b \in S(y)} \min_{a \in S(y')} ||b - a|| \} \quad (6)$$

where TP, FP, and FN refer to true positive predictions, false positive predictions, and false negative predictions. $S(y')$ and $S(y)$ indicate the boundary points on the predicted segmentations and reference segmentations.

Significant differences between the different experiments as well as between the model results and human annotations are determined using two-tailed paired t -tests with $P \leq 0.05$.

Results

Liver segmentation with severely limited annotations. Different sizes of high-quality annotated image samples are utilized to train the networks. As expected, more training samples lead to improved segmentation results (Fig. 3). Compared to networks trained with all the 10 labeled cases (331 image samples, DSC: 87.9%, RAVD: 10.4%, ASSD: 4.65mm, and MSSD: 65.1mm), the segmentation performance of networks trained with only 1 labeled case (30 image samples) is significantly worse (DSC: 70.1%, RAVD: 16.1%, ASSD: 16.1mm, and MSSD: 176.3mm). Thus, when the conventional training method is employed, large enough datasets with accurate labels are required to obtain satisfactory results.

To enlarge the training dataset, low-quality annotations are generated by the models trained with the few annotated training data. Then, networks are trained with the enlarged dataset. Table 1 lists the results under different training settings. Results indicate that our proposed AIDE can be

very effective when severely limited annotations are available. It achieves significantly better results compared to the baselines indicated by all the evaluation metrics. Particularly, with 30 labeled and 954 unlabeled training image samples, our method generates comparable results (DSC: 86.9%, RAVD: 10.0%, ASSD: 4.17mm, and MSSD: 44.6mm) to the models trained with 331 high-quality annotated samples (DSC: 88.5%, RAVD: 10.8%, ASSD: 3.64mm, and MSSD: 43.8mm) (no significant difference between the DSCs with $p = 0.0791$). Besides, it can be observed that with the increase of unlabeled training samples, our method continues to improve the model performance. Visualizations of the self-corrected annotations and model outputs are shown in Fig. 4. Overall, the annotations after correction are closer to the high-quality annotations, and our AIDE generates more accurate segmentations than the corresponding baseline networks.

Prostate segmentation lacking target domain annotations. By training with different domain datasets, the networks become biased with the domain properties, and the performance on data from other domains is compromised. Table 2 presents the results of networks tested on the same domain or different domains from the training set. Obvious reductions in the segmentation accuracy are observed when cross-domain testing is performed.

Fig. 5 presents the prostate segmentation results of models optimized without target domain training labels without or with the proposed AIDE framework. AIDE successfully improves the segmentation performance. As a special case, when transferring models from Domain 1 to Domain 2, direct model training with the combined dataset utilizing high-quality labels for Domain 1 and model generated low-quality labels for Domain 2 obtains even worse results (DSC: 33.7%, RAVD: 71.5%, ASSD: 5.94mm, and MSSD: 20.7mm) than those achieved by direct testing Domain 1 optimized models on Domain 2 data (DSC: 45.8%, RAVD: 65.6%, ASSD: 5.42mm, and MSSD:

17.8mm). On the other hand, AIDE increases the DSC by more than 30% (from 45.8% to 80.0%) and decreases other three metrics substantially. Nevertheless, even with AIDE, the performance on Domain 3 is still relatively worse than that on Domain 1 or Domain 2. Since Domain 3 is a combination of data from different sources, we speculate that adapting models to a combined dataset is more difficult. Overall, our experiments validate that the proposed framework achieves promising results on cross-domain model transfer without utilizing any target domain annotations.

Image segmentation with noisy annotations. Variations exist between annotations provided by different experts, especially for small target objects (Fig. 1). Overall, we found that AIDE can generate more consistent segmentation results distributions with the annotators by testing with different thresholds (Table 3). Even though the improvements on relatively large region segmentation tasks (task 1 for prostate segmentation and task 2 for brain growth segmentation) are minor, AIDE achieves substantially better performance on the more challenging small object segmentation tasks (task 3 for brain tumor segmentation and task 4 for kidney segmentation). Therefore, compared to the conventional methods that typically require more than 3 annotators to generate high-confidence annotations for generalizable testing performance, AIDE may relax the requirement.

Breast tumor segmentation on three independent collected clinical datasets. Experiments on the three breast tumor segmentation datasets validate the effectiveness of AIDE on analyzing clinical samples with decreased manual efforts. For all three datasets, our proposed AIDE, which utilizes less than 10% training annotations provided by the experienced radiologists, can generate similar segmentation performance to the corresponding fully supervised models (Fig. 6).

Specifically, for GGH dataset, AIDE achieves an average DSC of 0.690 ± 0.251 and the fully supervised model achieves 0.722 ± 0.208 ($P = 0.0608$). For GPPH, AIDE gets 0.654 ± 0.221 and the fully supervised model gets 0.678 ± 0.260 ($P = 0.2927$). For HPPH, AIDE obtains 0.731 ± 0.196 and the fully supervised model gets 0.738 ± 0.227 ($P = 0.6545$). It can be observed that AIDE performs better with larger datasets, which can be very useful in real clinical applications considering the large quantities of unannotated images accumulated every day.

Additional radiologists are employed to segment the breast tumors in the central slices of the three test sets. For GGH dataset, the manual annotations achieve an averaged DSC of 0.621 ± 0.155 , which is significantly worse than that of AIDE (0.690 ± 0.251) with $p = 0.0098$. For GPPH, the manual annotations get 0.861 ± 0.086 and AIDE gets 0.846 ± 0.118 . No significant difference is found ($p = 0.3317$). For HPPH, the manual annotations get 0.735 ± 0.225 and AIDE gets 0.761 ± 0.234 with no significant difference observed ($p = 0.3079$). Overall, it can be concluded that our proposed AIDE can generate comparable or even better segmentation results when compared with the radiologists.

Discussion

Image segmentation plays an important role in medical imaging applications. In research studies, DNNs have already been widely employed to automate and speed up the segmentation process. Despite the reported successful applications, the performance of DNNs depends heavily on the quality of the utilized training datasets. Building frameworks that can optimize DNNs without strict reliance on large and high-quality annotated training datasets can significantly narrow the gap between research works and clinical applications. In this study, we propose an annotation-efficient deep learning framework, AIDE, to handle the issue of medical image segmentation

network learning with imperfect datasets. Extensive experiments have been conducted with open datasets containing scarce and noisy annotations. Results show that AIDE performs substantially better than conventional models and even comparable to models trained with corresponding perfect datasets, thus validate the effectiveness of AIDE. Additional experiments on clinical breast tumor datasets from three medical centers further prove the robustness and generalization ability of AIDE when processing real clinical data. On all the three independent datasets, AIDE generates satisfactory segmentation results by utilizing only 10% training annotations, which indicates that AIDE can substantially alleviate radiologists' manual efforts compared to conventional DNNs.

The effectiveness of AIDE on handling low-quality annotated data can be attributed to its following advantages. First, the local label filtering step in each iteration enforces a constraint on suspected low-quality annotated samples to generate consistent predictions with those of the augmented inputs, which is a type of data distillation²². It can prevent the negative effects of low-quality annotations timely and in the meantime, exploit as much useful information as possible from these inputs instead of dropping them. Second, the global label correction step after each epoch progressively navigates the network towards predicting consistent results at different time points. In other words, the networks are expected to have small vibrations and those samples that lead to large vibrations are considered low-quality annotated samples that should be corrected. Direct label correction to replace the old labels offers the network a self-evolving capability. Since in most cases, medical images of the same regions look roughly similar among different patients, we believe that this evolving capability by updating a partial of suspected low-quality annotations is reasonable and feasible. The remaining non-updated samples can guarantee the stable training of the networks. Third, the cross-model co-optimization schedule can avoid the error propagation

and accumulation in one network. By building two networks and make them exchange information, we reduce the risk of network overfitting to its own predicted pseudo-labels.

Abundant existing works focus on DNN training with single types of imperfect datasets. Methods such as data augmentation^{18,23}, transfer learning^{19,20}, semi-supervised learning^{21,24}, and self-supervised learning^{25,26} have been extensively investigated to handle the issues of limited training annotations or no target domain annotations. On the other hand, much less attention has been paid to noisy label learning in medical imaging^{16,27}. Most of the existing studies concentrate on designing new loss weighting strategies^{28,29} or new loss functions³⁰. The most relevant available methods to ours are pseudo-labeling³¹ and co-teaching³². Compared to existing pseudo-labeling studies that update pseudo-labels of all unlabeled data simultaneously during network learning^{21,33,34}, label updating of AIDE is conducted in an orderly and selective manner according to an observed small loss criterion, which has also been noticed and confirmed for nature images³⁵. Moreover, AIDE trains the model with the segmentation loss on filtered labels to avoid the negative effects of highly noisy labels, and an additional consistency loss is introduced to enforce consistent predictions with augmented inputs for the remaining data. AIDE also differs from the two-model co-teaching method^{32,36} in which AIDE generates pseudo-labels for suspected low-quality annotated data in an effective and progressive manner from local to global instead of neglecting these data, which contributes to the full utilization of the valuable medical image data and improves the model performance.

Constructing large datasets with high-quality annotations is particularly challenging in medical imaging. Due to factors like patient privacy and institutional policies, the available data can be quite small for some situations. Moreover, medical image annotation, especially dense annotation for image segmentation, is very resource-intensive. Different from natural images, only

domain experts have the knowledge to annotate medical images. In some cases, such as our task on brain tumor segmentation, large variations exist between different experts, which raises the necessity of multiple annotators to achieve consensus annotations. Employing a large number of domain experts to annotate large medical image datasets can cost massive financial and logistical resources that are typically difficult to provide in many applications. Our proposed AIDE shows the potential to solve these issues effectively. It achieves satisfactory performance by utilizing only 10% of training annotations compared to the fully supervised counterparts. Nevertheless, label-free or unsupervised learning that can get rid of the manual annotations thoroughly is more appealing^{17,37}. We are still working on improving the methodology to further reduce the reliance on annotations. In our following study, we will seek to address the challenge of unsupervised deep learning for large scale and automatic medical image segmentation.

In summary, we have demonstrated that our proposed framework, AIDE, can achieve accurate medical image segmentation under severe training conditions with different kinds of imperfect training datasets. Therefore, it provides a new perspective for DNNs to handle imperfect datasets. On the clinical datasets, compared to conventional DNN training, it can save almost 90% manual effort on annotating the training data. With further development and clinical trials, such a 10-fold improvement of efficiency in utilizing experts' labels will promote a wide range of biomedical applications. Our proposed framework have the potential to improve the medical image diagnosing workflow in an efficient manner and at a low cost.

References

1. Bai, W. *et al.* A population-based phenome-wide association study of cardiac and aortic structure and function. *Nat. Med.* **26**, 1654–1662 (2020).

2. Mei, X. *et al.* Artificial intelligence-enabled rapid diagnosis of patients with COVID-19. *Nat. Med.* **26**, 1224–1228 (2020).
3. De Fauw, J. *et al.* Clinically applicable deep learning for diagnosis and referral in retinal disease. *Nat. Med.* **24**, 1342–1350 (2018).
4. Tang, H. *et al.* Clinically applicable deep learning framework for organs at risk delineation in CT images. *Nat. Mach. Intell.* **1**, 480–491 (2019).
5. Khened, M., Kollerathu, V. A. & Krishnamurthi, G. Fully convolutional multi-scale residual DenseNets for cardiac segmentation and automated cardiac diagnosis using ensemble of classifiers. *Med. Image Anal.* **51**, 21–45 (2019).
6. Litjens, G. *et al.* A survey on deep learning in medical image analysis. *Med. Image Anal.* **42**, 60–88 (2017).
7. Shen, D., Wu, G. & Suk, H.-I. Deep learning in medical image analysis. *Annu. Rev. Biomed. Eng.* **19**, 221–248 (2017).
8. Hesamian, M. H., Jia, W., He, X. & Kennedy, P. Deep learning techniques for medical image segmentation: Achievements and challenges. *J. Digit. Imaging* **32**, 582–596 (2019).
9. Li, X. *et al.* H-DenseUNet: Hybrid densely connected UNet for liver and tumor segmentation from CT volumes. *IEEE Trans. Med. Imaging* **37**, 2663–2674 (2018).
10. Dolz, J. *et al.* HyperDense-Net: A hyper-densely connected CNN for multi-modal image segmentation. *IEEE Trans. Med. Imaging* **38**, 1116–1126 (2019).
11. Haberl, M. G. *et al.* CDeep3M—Plug-and-Play cloud-based deep learning for image segmentation. *Nat. Methods* **15**, 677–680 (2018).
12. Lecun, Y., Bengio, Y. & Hinton, G. Deep learning. *Nature* **521**, 436–444 (2015).
13. Webb, S. Deep learning for biology. *Nature* **554**, 555–557 (2018).

14. Lutnick, B. *et al.* An integrated iterative annotation technique for easing neural network training in medical image analysis. *Nat. Mach. Intell.* **1**, 112–119 (2019).
15. Tajbakhsh, N. *et al.* Embracing imperfect datasets: A review of deep learning solutions for medical image segmentation. *Med. Image Anal.* **63**, 101693 (2020).
16. Karimi, D., Dou, H., Warfield, S. K. & Gholipour, A. Deep learning with noisy labels: exploring techniques and remedies in medical image analysis. *Med. Image Anal.* **65**, 101759 (2020).
17. Esteva, A. *et al.* A guide to deep learning in healthcare. *Nat. Med.* **25**, 24–29 (2019).
18. Zhang, Z., Yang, L. & Zheng, Y. Translating and segmenting multimodal medical volumes with cycle- and shape-consistency generative adversarial network. in *IEEE Conference on Computer Vision and Pattern Recognition (CVPR)* 9242–9251 (IEEE, 2018).
19. Chen, C., Dou, Q., Chen, H., Qin, J. & Heng, P. A. Unsupervised bidirectional cross-modality adaptation via deeply synergistic image and feature alignment for medical image segmentation. *IEEE Trans. Med. Imaging* **39**, 2494–2505 (2020).
20. Wang, Y. *et al.* Augmenting vascular disease diagnosis by vasculature-aware unsupervised learning. *Nat. Mach. Intell.* **2**, 337–346 (2020).
21. Nie, D., Gao, Y., Wang, L. & B, D. S. ASDNet: attention based semi-supervised deep networks for medical image segmentation. in *International Conference on Medical Image Computing and Computer Assisted Intervention - MICCAI 2018* **11073**, 370–378 (Springer, Cham, 2018).
22. Vohra, Y. *et al.* Data distillation: towards omni-supervised learning. in *IEEE Conference on Computer Vision and Pattern Recognition (CVPR)* 4119–4128 (IEEE, 2018).

23. Li, Z., Kamnitsas, K. & Glocker, B. Overfitting of neural nets under class imbalance: analysis and improvements for segmentation. in *International Conference on Medical Image Computing and Computer Assisted Intervention - MICCAI 2019* **11766**, 402–410 (Springer, Cham, 2019).
24. Ren, X. *et al.* Interleaved 3D-CNNs for joint segmentation of small-volume structures in head and neck CT images. *Med. Phys.* **45**, 2063–2075 (2018).
25. Bai, W. *et al.* Self-supervised learning for cardiac MR image segmentation by anatomical position prediction. in *International Conference on Medical Image Computing and Computer Assisted Intervention - MICCAI 2019* **11765**, 541–549 (Springer, Cham, 2019).
26. Zhou, Z. *et al.* Models genesis: generic autodidactic models for 3d medical image analysis. in *International Conference on Medical Image Computing and Computer Assisted Intervention - MICCAI 2019* **11767**, 384–393 (Springer, Cham, 2019).
27. Hardt, M. Understanding deep learning requires rethinking generalisation. in *International Conference on Learning Representations (ICLR)* 1–15 (2017).
28. Le, H. *et al.* Pancreatic cancer detection in whole slide images using noisy label annotations. in *International Conference on Medical Image Computing and Computer Assisted Intervention - MICCAI 2019* **11764**, 541–549 (Springer, Cham, 2019).
29. Zhu, H., Shi, J. & Wu, J. Pick-and-learn: automatic quality evaluation for noisy-labeled image segmentation. in *International Conference on Medical Image Computing and Computer Assisted Intervention - MICCAI 2019* **11769**, 576–584 (Springer, Cham, 2019).
30. Liu, C., B, H. X., Liu, Y., Zha, Z. & Lin, F. LVC-Net: medical image segmentation with noisy label based on local visual cues. in *International Conference on Medical Image*

- Computing and Computer Assisted Intervention - MICCAI 2019* **11769**, 558–566 (Springer, Cham, 2019).
31. Lee, D.-H. Pseudo-label: The simple and efficient semi-supervised learning method for deep neural networks. *ICML 2013 Work. Challenges Represent. Learn.* 1–6 (2013).
 32. Han, B. *et al.* Co-teaching: Robust training of deep neural networks with extremely noisy labels. in *Conference on Neural Information Processing Systems (NeurIPS)* (2018).
 33. Bai, W. *et al.* Semi-supervised learning for network-based cardiac MR image segmentation. in *International Conference on Medical Image Computing and Computer Assisted Intervention - MICCAI 2017* **10434**, 253–260 (Springer, Cham, 2017).
 34. Xia, Y. *et al.* 3D semi-supervised learning with uncertainty-aware multi-view co-training. in *Winter Conference on Applications of Computer Vision (WACV)* 3646–3655 (2020).
 35. Arplt, D. *et al.* A closer look at memorization in deep networks. in *International Conference on Machine Learning (ICML)* (2017).
 36. Yu, X. *et al.* How does disagreement help generalization against label corruption? in *International Conference on Machine Learning (ICML)* (2019).
 37. Greenspan, H., Ginneken, B. van & Summers, R. M. Deep learning in medical imaging: Overview and future promise of an exciting new technique. *IEEE Trans. Med. Imaging* **35**, 1153–1159 (2016).
 38. Kavur, A. E. *et al.* CHAOS challenge - combined (CT-MR) healthy abdominal organ segmentation. *arXiv pre-print* 1–10 (2020).
 39. Kavur, A. E. *et al.* Comparison of semi-automatic and deep learning-based automatic methods for liver segmentation in living liver transplant donors. *Diagnostic Interv. Radiol.* **26**, 11–21 (2020).

40. Kavur, A. E., Selver, M. A., Dicle, O., Barış, M. & Gezer, N. S. CHAOS - combined (CT-MR) healthy abdominal organ segmentation challenge data. *Zenodo* (2019).
41. NCI-ISBI 2013 challenge: automated segmentation of prostate structures. (2013).
42. Litjens, G. *et al.* Evaluation of prostate segmentation algorithms for MRI: The PROMISE12 challenge. *Med. Image Anal.* **18**, 359–373 (2014).
43. Jiang, L., Zhou, Z., Leung, T., Li, L. J. & Fei-Fei, L. MentorNet: Learning data-driven curriculum for very deep neural networks on corrupted labels. in *International Conference on Machine Learning (ICML)* (2018).
44. Chen, P., Liao, B., Chen, G. & Zhang, S. Understanding and utilizing deep neural networks trained with noisy labels. in *International Conference on Machine Learning (ICML)* (2019).
45. Falk, T. *et al.* U-Net: deep learning for cell counting, detection, and morphometry. *Nat. Methods* **16**, 67–70 (2019).
46. Hazirbas, C. & Ma, L. FuseNet: Incorporating depth into semantic segmentation via fusion-based CNN architecture. in *Asian Conference on Computer Vision (ACCV)* (2016).
47. Li, C. *et al.* Learning cross-modal deep representations for multi-modal MR image segmentation. in *International Conference on Medical Image Computing and Computer Assisted Intervention - MICCAI 2019* **11765**, 57–65 (Springer, Cham, 2019).

Data availability. The raw image data and relevant information of the utilized open datasets are accessible from the respective official websites of the challenges (CHAOS: <https://chaos.grand-challenge.org/>, NCI-ISBI 2013: <https://wiki.cancerimagingarchive.net/display/Public/NCI-ISBI+2013+Challenge+-+Automated+Segmentation+of+Prostate+Structures>, PROMISE12: <https://promise12.grand-challenge.org/>, and QUBIQ: <https://qubiq.grand-challenge.org/>) through standard procedures. The clinical breast data were collected by the hospitals in de-identified format. They are not publicly available and restrictions apply to their use.

Code availability. The code used for training the deep-learning models and models used in this study will be made available at <https://github.com/lich0031/AIDE>. Implementation of our work is based on PyTorch with necessary publicly available packages, such as numpy, PIL, and SimpleITK.

Acknowledgements

We would like to thank all the participants and staff of the four challenges, CHAOS, NCI-ISBI 2013, PROMISE12, and QUBIQ. This work was partly supported by Scientific and Technical Innovation 2030-“New Generation Artificial Intelligence” Project (2020AAA0104100, 2020AAA0104105), the National Natural Science Foundation of China (61871371, 81830056), Key-Area Research and Development Program of Guangdong Province (2018B010109009), the Basic Research Program of Shenzhen (JCYJ20180507182400762), Youth Innovation Promotion Association Program of Chinese Academy of Sciences (2019351, National Key R&D Program of China (2017YFE0103600), National Natural Science Foundation of China (81720108021),

Zhongyuan Thousand Talents Plan Project (ZYQR201810117), Zhengzhou Collaborative Innovation Major Project (20XTZX05015).

Author contributions

S.S.W and C.L. proposed the idea, initialized the project and the collaboration. C.L. and S.S.W developed and implemented the framework. R.P.W., Z.Y.L., M.Y.W., H.N.T., and X.F.L. collected the breast data. R.P.W., Z.Y.L., M.Y.W., Y.P.W., and R.Y. provided the manual annotations. R.P.W., Z.Y.L., M.Y.W., H.N.T., X.F.L., Y.P.W., R.Y., and X.L. contributed clinical expertise. C.L. and H.S analyzed the results and plotted the figures. C.L., H.S., I.B.A., H.C.P., and S.S.W. wrote the manuscript. S.S.W., H.R.Z, and H.C.P. supervised the project. All authors read and contributed to revision and approved the manuscript.

Competing interests

The authors have no competing interests to disclose.

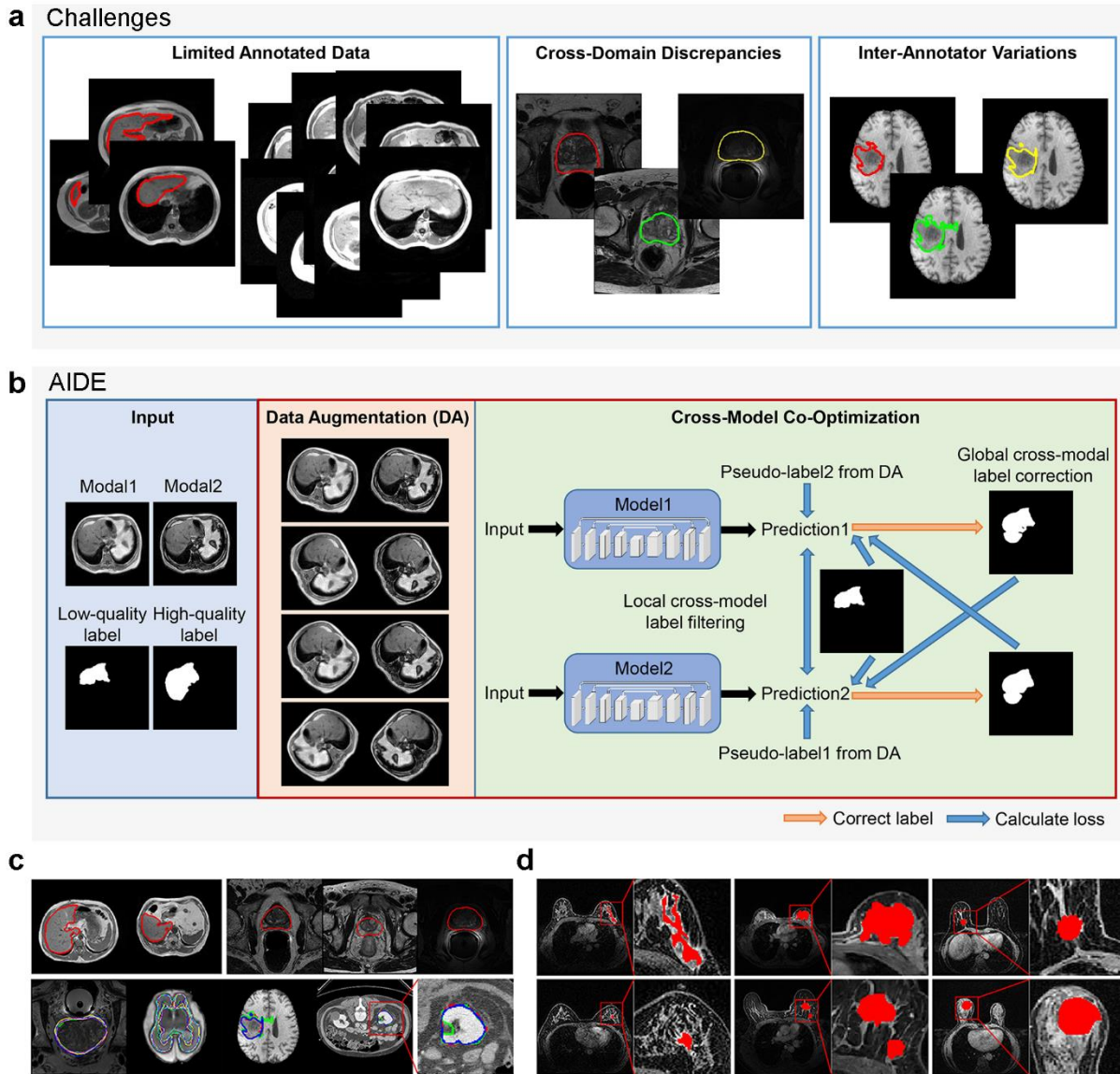


Fig. 1 | Overview of AIDE. **a**, The three challenging tasks relevant to imperfect datasets. **b**, The overall framework of AIDE with three major elements, the local label filtering, the global label correction, and the cross-model co-optimization. **c**, Example images of the open datasets. Top left two images are from CHAOS dataset. Top right three images are from the three prostate datasets with different domain characteristics. Bottom images are from the QUBIQ datasets with the first four images correspond to the four subtasks and the last one is an enlarged view of the fourth image. Color lines indicate the regions to be segmented. **d**, Example images of the collected breast tumor datasets. From left to right, the three columns correspond to the images collected from the three medical centers. Red color regions show the breast tumors.

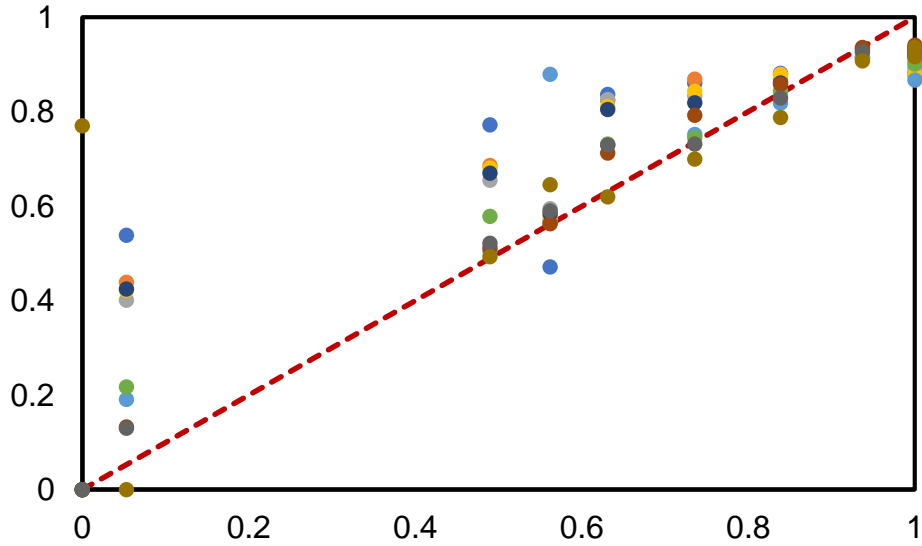


Fig. 2 | Positive correlation between the DSCs calculated comparing network outputs to current noisy labels (vertical axis) and the DSCs calculated comparing current noisy labels to the high-quality labels (horizontal axis) for the training set. Different colored data points refer to the results at different training epochs.

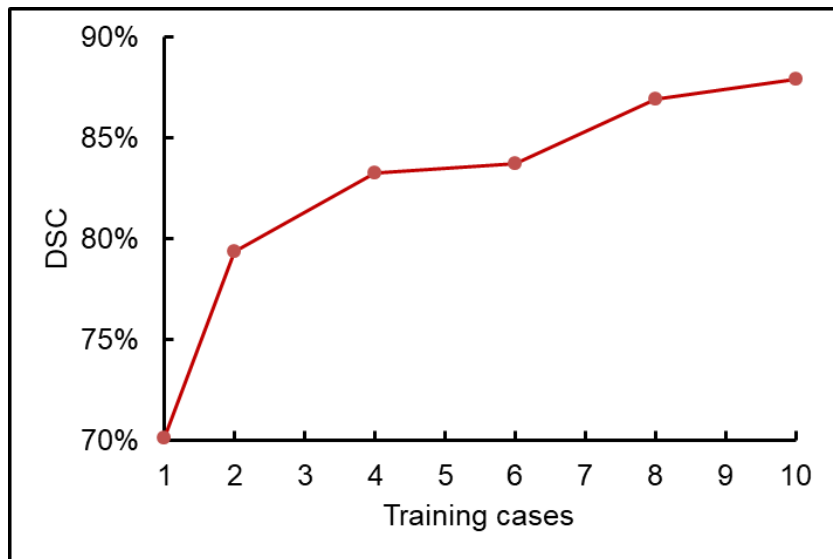


Fig. 3 | Network performance on the test set (characterized by Dice score) with 1, 2, 4, 6, 8, or 10 training cases with high-quality labels of the CHAOS dataset. More training samples lead to improved segmentation performance

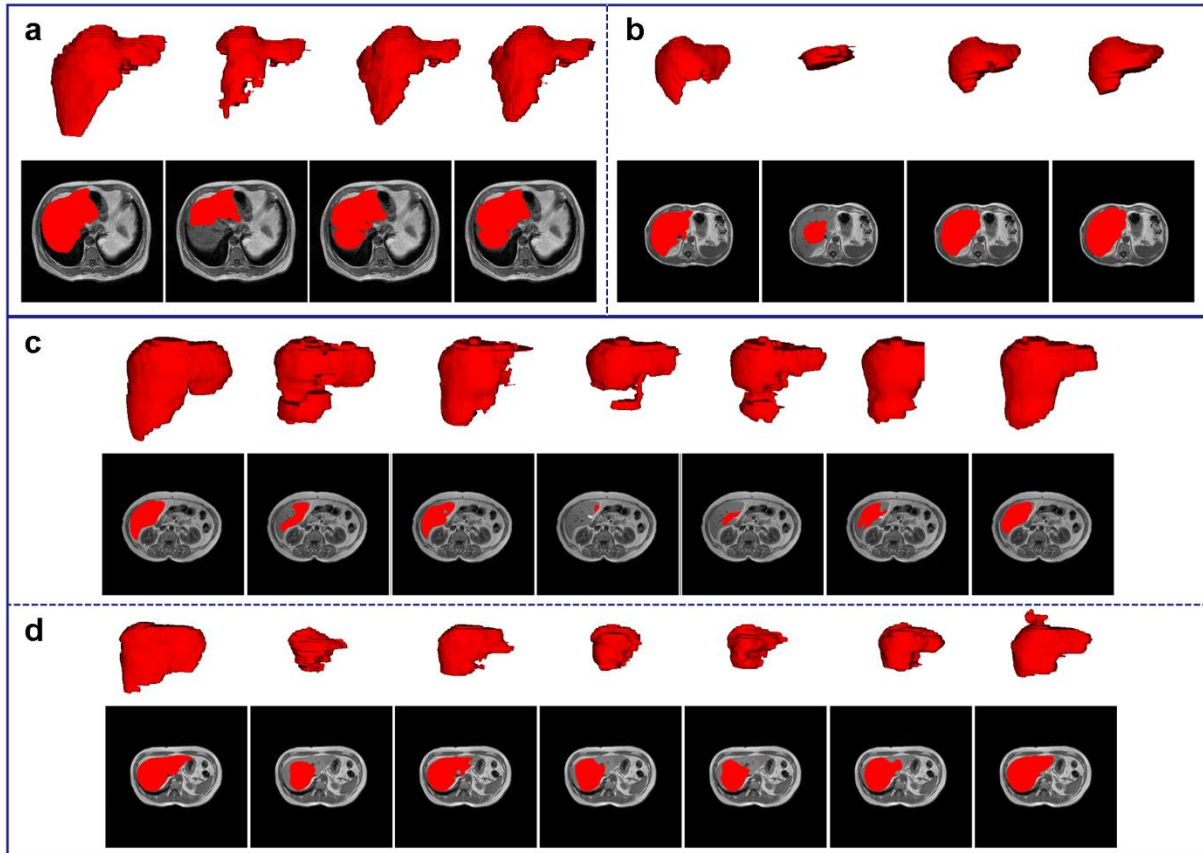


Fig. 4 | Visualization of label correction and segmentation results. **a** and **b**, two cases of the training data label correction results. The red color regions in the four images from left to right correspond to the high-quality label, the low-quality label utilized to train the model, the self-corrected labels of the two networks, respectively. **c** and **d**, two cases of the segmentation results. The first columns are the corresponding high-quality labels. The second to the last columns are the results achieved under settings S02, S04, S06, S08, S10, and S12 in Table 1.

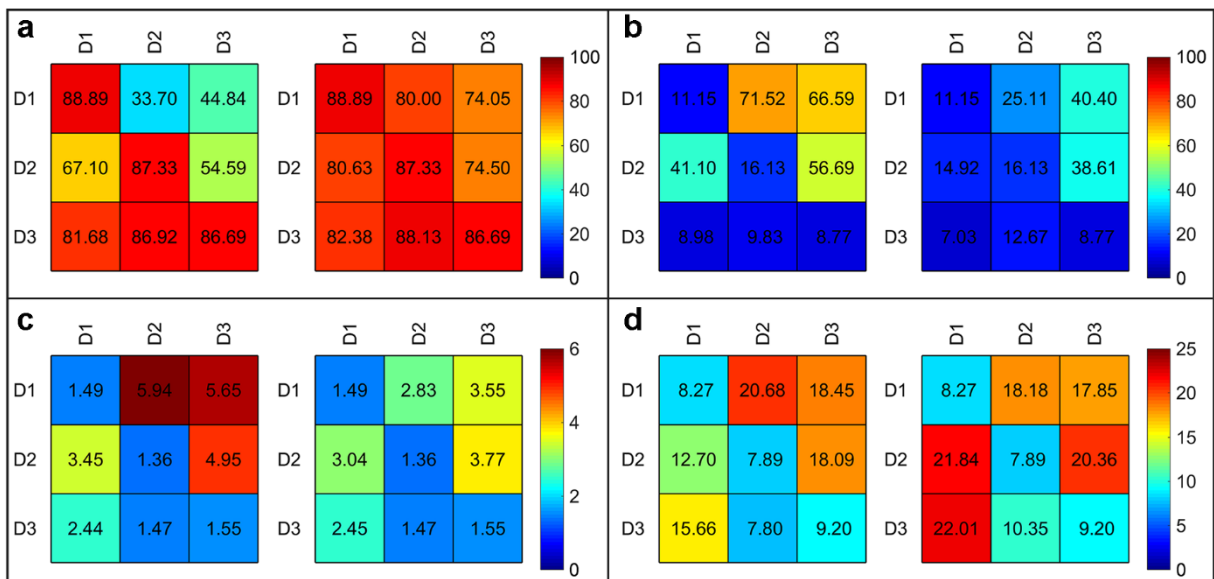


Fig. 5 | Results of prostate segmentation lacking target domain annotations. a, b, c, and d, the four evaluation metrics, DSC (%), RAVD (%), ASSD (mm), and MSSD (mm). In each sub-figure, the left and right mappings indicate that the networks are trained without and with the proposed AIDE. D1, D2, and D3 refer to Domain 1, 2, and 3. In each mapping, y axis indicates the dataset utilized to train the models and x axis indicates the dataset utilized to test the models.

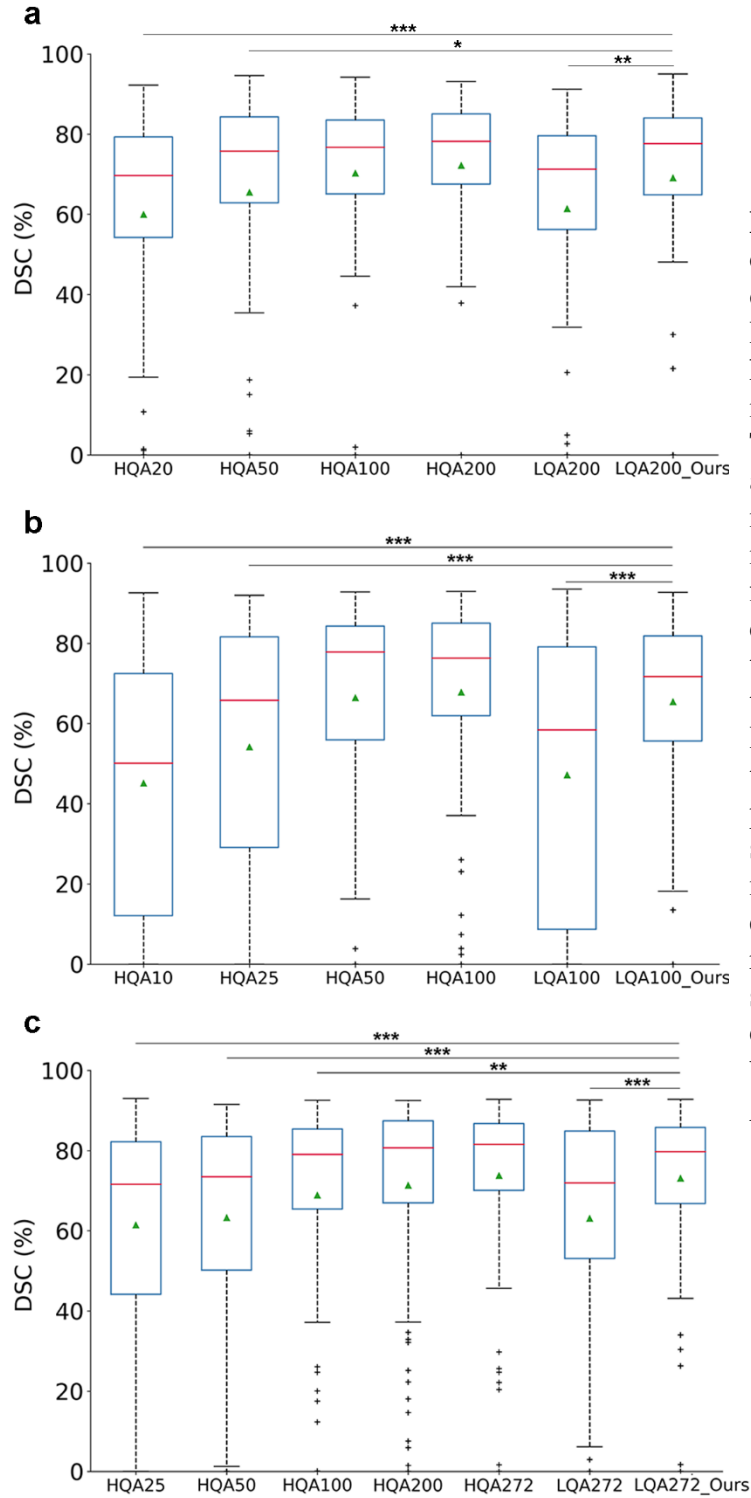


Fig. 6 | Segmentation performance on the clinical datasets. a, Results on GGH. **b**, Results on GPPH. **c**, Results on HPPH. HQA indicates high-quality annotations. LQA indicates low-quality annotations. The numbers after HQA refers to the annotations utilized to train the models. For LQA, the numbers indicate that we utilize the respective fewest HQA data (20 cases for **a**, 10 cases for **b**, and 25 cases for **c**) with the rest annotations generated by the trained models (HQA20 for **a**, HQA10 for **b**, and HQA25 for **c**). All the training data numbers reflect the patient counts instead of image samples. The red lines indicate the median DSC values of the experiments and the green triangles refer to the average values. * means significant difference between the corresponding experiments evaluated by paired *t*-tests. *** $P \leq 0.001$, ** $P \leq 0.005$, and * $P \leq 0.05$.

Table 1 | Segmentation results of networks under different training settings

Settings	Train HQA	Train LQA	AIDE	Post- processing	DSC (%)	RAVD (%)	ASSD (mm)	MSSD (mm)
S01	30	0	No	No	70.1	42.0	16.1	176.3
S02	30	0	No	Yes	75.6	22.0	7.68	54.8
S03	331	0	No	No	87.9	10.4	4.65	65.1
S04	331	0	No	Yes	88.5	10.8	3.64	43.8
S05	30	301	No	No	78.4	19.0	7.92	95.3
S06	30	301	No	Yes	79.7	21.1	6.10	53.4
S07	30	301	Yes	No	79.8	18.5	10.8	116.3
S08	30	301	Yes	Yes	82.9	16.9	5.43	49.8
S09	30	954	No	No	79.5	19.7	8.43	104.2
S10	30	954	No	Yes	80.2	19.1	6.47	53.8
S11	30	954	Yes	No	86.1	10.2	5.49	75.8
S12	30	954	Yes	Yes	86.9	10.0	4.17	44.6

Bold numbers indicate the results achieved by our final AIDE. HQA indicates high-quality training annotations. LQA indicates low-quality training annotations where the annotations are generated by respective models trained with the provided high-quality annotated samples. Post-processing refers to the process of keeping the largest connected components

Table 2 | Segmentation results of networks with prostate datasets. Cross-domain testing decreases the network performance significantly.

Training dataset	Testing dataset	DSC (%)	RAVD (%)	ASSD (mm)	MSSD (mm)
Domain 1	Domain 1	88.9	11.1	1.49	8.27
Domain 1	Domain 2	45.8	65.6	5.42	17.8
Domain 1	Domain 3	40.0	67.8	9.24	24.3
Domain 2	Domain 1	69.8	35.5	3.43	12.9
Domain 2	Domain 2	87.3	16.1	1.36	7.89
Domain 2	Domain 3	55.1	53.0	8.32	21.3
Domain 3	Domain 1	80.9	8.61	2.43	14.9
Domain 3	Domain 2	86.1	12.3	1.58	8.27
Domain 3	Domain 3	86.7	8.77	1.55	9.20

Table 3 | Segmentation performance (DSC: %) on the QUBIQ datasets

Task1_Prostate Segmentation							
Method	Anno1	Anno2	Anno3	Anno4	Anno5	Anno6	
Conventional	89.2	87.9	84.3	89.3	86.4	90.0	
AIDE	91.4	89.2	85.2	90.4	88.1	90.3	
Task2_Brain Growth Segmentation							
Method	Anno1	Anno2	Anno3	Anno4	Anno5	Anno6	Anno7
Conventional	70.7	73.2	73.8	73.2	71.6	72.1	71.8
AIDE	71.1	75.0	74.8	73.5	71.6	72.7	72.0
Task3_Brain Tumor Segmentation				Task4_Kidney Segmentation			
Method	Anno1	Anno2	Anno3	Method	Anno1	Anno2	Anno3
Conventional	83.9	83.1	84.2	Conventional	69.8	68.9	70.7
AIDE	92.6	91.8	92.7	AIDE	85.4	83.8	89.9

Algorithm 1 | Cross-Model Self-Correcting Mechanism of AIDE.

```
1: Input Net1 (N1 with parameter  $w_1$ ) and Net2 (N2 with parameter  $w_2$ ), learning rate  $lr$ ,
training set  $D$ , batch size  $B$ , number of augmentations  $K$ , Sharpening temperature  $T$ ,
Segmentation loss function  $L_{seg}$ , Consistency loss function  $L_{con}$ , Loss weight  $\lambda$ , Label
update ratio  $R$ , Label update criterion  $U$ , Warm up epoch  $q_w$ , and total epoch  $Q$ 
2: for  $q = 1, 2, \dots, Q$  do
3:   Shuffle training set  $D$  into  $|D|/B$  min batches;
4:   for  $n = 1$  to  $|D|/B$  do
5:     Fetch batch inputs  $d = ((x_b, y_{b1}, y_{b2}); b \in (1, \dots, B))$  from  $D$ 
      ( $y_{b1}, y_{b2}$ : references for N1 and N2, initialized to be the low-quality annotations);
6:     for  $b = 1$  to  $B$  do
7:       for  $k = 1$  to  $K$  do
8:         Obtain  $\hat{x}_{b1} = \text{Augment}(x_b)$ 
9:       end for
10:       $\bar{y}_{b1} = \frac{1}{K} \sum_k (N_1(y | \hat{x}_b; w_1))$ 
11:       $\hat{y}_{b1} = \text{Sharpen}(\bar{y}_{b1}, T)$ 
12:       $\bar{y}_{b2} = \frac{1}{K} \sum_k (N_2(y | \hat{x}_b; w_2))$ 
13:       $\hat{y}_{b2} = \text{Sharpen}(\bar{y}_{b2}, T)$ 
14:    end for
15:    Obtain local accurately annotated samples  $d_{s1} = \text{argmin}_{d' \in d: |d'| \leq 0.5B} L_{seg}(d', w_1)$ 
16:    Obtain local accurately annotated samples  $d_{s2} = \text{argmin}_{d' \in d: |d'| \leq 0.5B} L_{seg}(d', w_2)$ 
17:    Obtain  $L1 = L_{seg}(d_{s2}; w_1) + (1.0 - \lambda_q) L_{seg}(d_{l2}; w_1) + \lambda_q L_{con}(d_{l2}; w_1)$ ,  $d_{l1} = d / d_{s1}$ 
18:    Obtain  $L2 = L_{seg}(d_{s1}; w_2) + (1.0 - \lambda_q) L_{seg}(d_{l1}; w_2) + \lambda_q L_{con}(d_{l1}; w_2)$ ,  $d_{l2} = d / d_{s2}$ 
19:    Update  $w_1 = w_1 - lr \nabla L1$ 
20:    Update  $w_2 = w_2 - lr \nabla L2$ 
21:  end for
22:  Update  $\lambda_q = \min\{\lambda * L(q / q_t)^2, \lambda\}$ ,  $\lambda = 1.0$ 
23:  Obtain global noisily annotated samples  $D_{l1} = \text{argmin}_{D' \in D: |D'| \leq R} \text{Dice}(D', w_1)$ 
24:  Obtain global noisily annotated samples  $D_{l2} = \text{argmin}_{D' \in D: |D'| \leq R} \text{Dice}(D', w_2)$ 
25:  if  $U$  do
26:    Update  $y_{b2} = N_1(y | D_{l1}; w_1)$ 
27:    Update  $y_{b1} = N_2(y | D_{l2}; w_2)$ 
28:    Obtain  $DSC_{train} = \text{mean}(\text{Dice}(D, w_1), \text{Dice}(D, w_2))$ 
29:  end if
30: end for
31: Output  $w_1$  and  $w_2$  with the highest  $DSC_{train}$ 
```